Unraveling the intrinsic atomic physics behind x-ray absorption line shifts in warm dense silicon plasmas

Valentin V. Karasiev[1,*] and S. X. Hu[1]

[1] *Laboratory for Laser Energetics, University of Rochester, 250 East River Road, Rochester, New York 14623 USA*

(Dated: February 12, 2021)

We present a novel free-energy density functional theory (DFT)-based methodology for optical property calculations of warm dense matter to cover a wide range of thermodynamic conditions and photon energies including the entire x-ray range. It uses Mermin–Kohn–Sham density functional theory with exchange-correlation (XC) thermal effects taken into account via a fully temperature dependent generalized gradient approximation XC functional. The methodology incorporates a combination of the *ab initio* molecular dynamics (AIMD) snapshotted Kubo–Greenwood optic data with a single-atom in simulation cell calculations to close the photon energy gap between the L and K edges and extend the K-edge tail toward many-keV photon energies. This gap arises in the standard scheme due to a prohibitively large number of bands required for the Kubo–Greenwood calculations with AIMD snapshots. Kubo–Greenwood data on snapshots provide an accurate description of optic properties at low photon frequencies slightly beyond the L-edge and x-ray absorption near edges structure (XANES) spectra, while data from periodic calculations with single atoms cover the tail regions beyond the edges. To demonstrate its applicability to mid-Z materials where the standard DFT-based approach is not computationally feasible, we have applied it to opacity calculations of warm dense silicon plasmas. These *first-principles* calculations revealed a very interesting phenomon of red-to-blue shift in K–L ($1s \rightarrow 2p$) and K-edge absorptions along both isotherm and isochore, which are absent in most continuum-lowering models of traditional plasma physics. This new physics phenomenon can be attributed to the underlying competition between the screening of deeply bound core electrons and the screening of outer-shell electrons caused by warm-dense-plasma conditions. We further demonstrate that the ratio of $1s \rightarrow 2p$ to the K-edge x-ray absorptions can be used to characterize warm-dense-plasma conditions. Eventually, based on our absorption calculations, we have established a *first-principles* opacity table (FPOT) for silicon in a wide range of material densities and temperatures.

PACS numbers:

I. INTRODUCTION

Accurate knowledge of radiative properties of matter in a wide range of material densities across different temperature regimes is of growing importance in many areas of research such as planetary science, astrophysics, and inertial confinement fusion (ICF) [1–4]. The traditional opacity models based on isolated atomic physics with plasma effect corrections [5–13], which are often reliable and frequently used at low density and hot plasma conditions, can be called into question when applied to warm dense and superdense plasmas [14–19]. For instance, significant discrepancy between experimental opacity measurements of transition metals at the solar corona conditions and traditional opacity models has been recently revealed [14, 19], while good agreement was seen in relatively low densities. The incompletion of our current understanding of atomic physics in dense plasmas has also been exampled by recent measurements of the ionization potential depression (IPD) in warm/hot dense aluminum plasmas [20–22], which have called into question the traditional continuum-lowering plasma physics models such as Ecker–Kröll [23] and Stewart–Pyatt [24]. Later these experimental data were reanalyzed with an alternative approach suitable for the analysis of IPD of solid density plasmas. The atomic-solid-plasma (APS) model developed in Ref. [25] identified the importance of a remaining crystal structure and explained these IPD measurement data.

A different approach to understand the intrinsic atomic physics and radiative properties of dense plasmas relies on quantum mean-field theory such as density functional theory (DFT) and Hartree–Fock–Slater-type modeling [26–28]. Recent DFT calculations of continuum lowering in strongly coupled aluminum and compound plasmas [27, 28] have shown some success in comparison with experiments while revealing the inadequacy of standard plasma models at warm dense conditions. However, these simplified DFT calculations adopted approximations of using a projector augmented wave (PAW) data set with K- and L-shell electrons frozen in the core.

A fully self-consistent calculation of the IPD effect on $1s$ electrons and related K-edge location requires invoking deeply bounded core electrons with the bare Coulomb potential or an *all-active-electron* PAW data set [29–32]. Using this approach, a free-energy DFT realized

*Electronic address: vkarasev@lle.rochester.edu

via orbital-dependent Mermin–Kohn–Sham [33] or via orbital-free (OF) [34–38] schemes for electronic degrees of freedom can be coupled to drive *ab-initio* molecular dynamics (AIMD) for ionic motion in dense plasmas. It can naturally take into account ionization degree, screening by both bound and free electrons, and interaction among neighboring ions self-consistently [16, 29–32, 39]. However, the orbital-based form of this *first-principles* approach, when applied to calculation of optical properties, requires explicitly handling deeply bounded core electrons in an equal footing with free electrons in the system. This requirement has posed great challenges on fully self-consistent DFT calculations of optical properties of warm dense matter, in particular for mid-Z materials at a wide range of x-ray photon energies.

In this work, we develop a novel methodology based on *all-electron* DFT for calculating the optical properties of warm dense plasmas of mid-Z materials in a broad range of x-ray photon energies (up to $h\nu \sim 10$ keV). To demonstrate its applicability, we have used this novel method to systematically calculate the x-ray absorption of dense silicon plasmas for a wide range of densities and temperatures ($\rho = 0.5$ to 500 g/cm^3 and $T = 5 \times 10^3$ to 10^7 K). Based on these data, a *first-principles* opacity table (FPOT) of silicon has been built for inertial confinement fusion (ICF) and high-energy-density physics (HEDP) applications. These *ab-intio* results revealed interesting trends of density/temperature-induced red-to-blue shifts of K edge and $1s \rightarrow 2p$ absorption lines along both the isotherm and isochore. These absorption line shifts provide an ubiquitous measure of the competition between screening of deep bound electrons and screening of outer-shell electrons due to the warm-dense-plasma environment. Comparisons with existing atomistic models show significant differences, with most of the traditional plasma-physics models incapable of predicting the DFT-predicted red shifts of absorption lines. Furthermore, our data indicate that one can use the absorption ratio of $1s \rightarrow 2p$ to K edge for characterizing thermodynamic conditions of warm dense plasmas through x-ray spectroscopy measurements [40–44] coupled with DFT calculations.

The next section introduces the methodology developed in our present work. Computational details are presented in Sec. III. Sections IV A and IV B describe our main results for absorption and opacity, and Sec. V provides a short summary and conclusions.

II. NOVEL METHODOLOGY TO CALCULATE X-RAY OPTICAL PROPERTIES

The Kubo–Greenwood formalism [45, 46] in combination with Kohn–Sham DFT is a *first-principles* approach to calculate transport properties of standard condensed-matter systems and dense plasmas. Within this approach, all bound and free electrons are treated on equal footing and contributions of the bound-bound, bound-free, and free-free transitions are naturally taken into account. Calculations performed on an uncorrelated sample set of fixed ionic configurations selected along molecular dynamics trajectory (so-called snapshotting) take into account effects due to the local ionic environment and are successful to describe x-ray absorption near edges structure (XANES) spectra [30, 40]. For this method to work, a large number of empty bands must be included into calculations to cover photon energies up to the x-ray range; bare Coulomb or an all-electron pseudo-potential for explicit treatment of all electrons including deep $1s$ states require a high plane-wave energy cutoff. All of these in conjunction with a large real-space size simulation cell in the case of low material density and/or a large number of atoms usually make such calculations prohibitively expensive even on today's high-performance computers.

To illustrate this challenge, we show in Figs. 1(a) and 1(b) a typical situation when the number of bands included in the DFT electronic structure and Kubo–Greenwood optical calculations were not enough to close the gap between L and K edges and to extend the photon energy range above 2 keV. For this example, we consider warm dense silicon at $\rho = 5.0$ g/cm^3 and $T = 250$ kK, for which absorption coefficients are calculated in a supercell of 32 atoms with 4096 bands. The resulting spectra [blue dashed line in Fig. 1(a)] show a sharp drop to zero for both the L-edge tail at $h\nu \sim 400$ eV and the K-edge tail at $h\nu \sim 2100$ eV. This is caused by the fact that not enough empty bands were involved in the calculation, i.e., there were not enough continuum states for $1s$ and $2p/2s$ electrons to transition to. Simply increasing the number of bands (N) is not a viable way to go because the cost of DFT calculations scales as $\sim N^3$ and such a calculation will require $N \approx 500,000$ to continuously cover the photon energy range up to 10 keV!

To circumvent this difficulty, we propose to combine the usual supercell MD results with a *single-atom-in-a-cell* calculation at the same thermodynamic conditions with the same periodic boundary condition. Note that for the same number of bands the *single-atom-in-a-cell* calculation can cover much wider photon energy range because of the high-energy continuum states that can be invoked. Since short-wavelength (large-$h\nu$) interactions mainly probe the local atomic/plasma environment, *single-atom-in-a-cell* calculations can give reasonably good results for high-energy photon absorptions. For instance, in Fig. 1(a) there is an overlap between supercell molecular dynamics (MD) results (blue dashed line marked as "Si_{32}") and the *single-atom-in-a-cell* calculation (black curve marked as "Si_1") in the range of photon energies above the L edge ($h\nu \sim 200$ to 400 eV), indicating an excellent agreement between these two calculations for the L-edge tail. Therefore, the *single-atom-in-a-cell* results can close the gap between L and K edges,

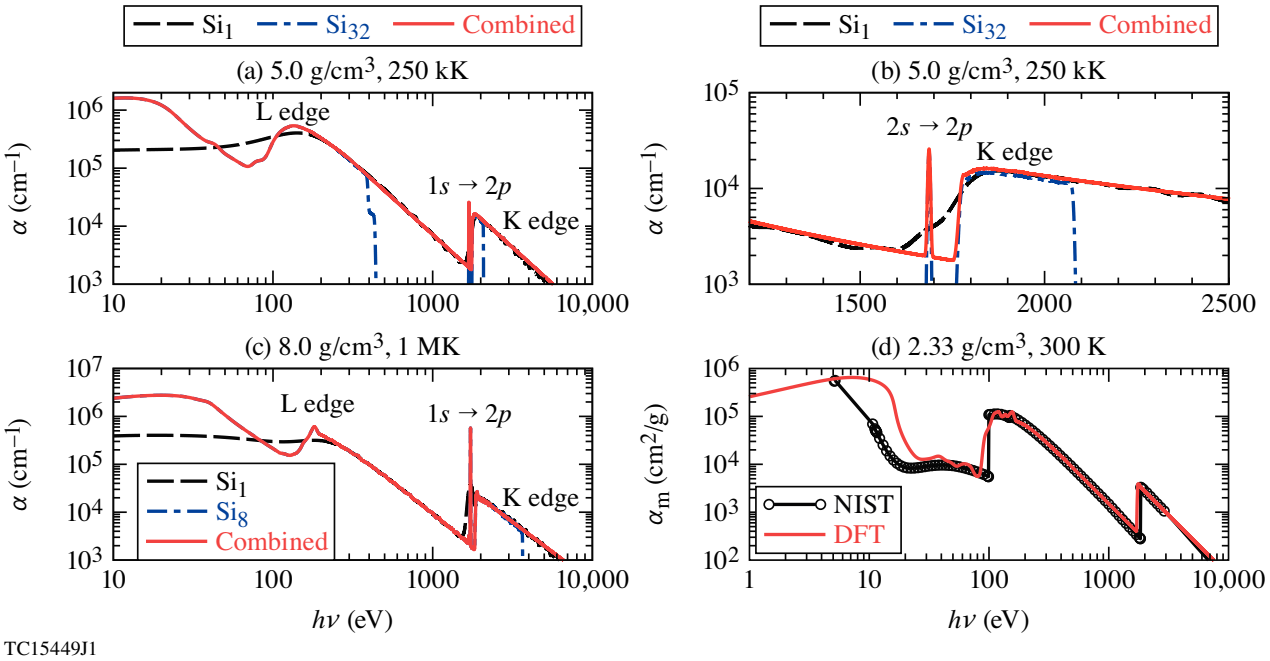

FIG. 1: [(a),(b)] Absorption of silicon plasmas at $\rho = 5.0$ g/cm^3 and $T = 250$ kK from calculations for a *single-atom-in-a-cell* (black dashed curve), calculations along the MD trajectory (dashed–dotted blue curve), and final combined results (solid red curve); (c) comparison between absorption calculated along the MD trajectory and data combined according to our methodology for $\rho = 8.0$ g/cm^3 and $T = 1$ MK; (d) comparison between the mass absorption coefficient calculated by the present method for $\rho = 2.33$ g/cm^3 and $T = 300$ K and NIST "cold solid" data for silicon (ambient conditions).

as shown in Fig. 1(a). For comparison, standard isolated atomic single particle models can describe reasonably well the K-shell photoionization [see Ref. [47] and citations therein]; however the calculated L- and M-shell photoionization cross sections differ from experimental values due to multi-electron correlations play an important role [48].

Zooming in on the K-edge range in Fig. 1(b), we find the supercell MD result produces the strong $1s \to 2p$ absorption line at ∼1700 eV and the K edge. However, it does not include a "background" absorption due to the missing L-edge tail; this is why the MD snapshot dashed–dotted blue line in Fig. 1(b) lies slightly below the dashed black line, which includes all bound-free transitions. This L-edge tail background absorption is extracted from the *single-atom-in-cell* results in simple analytical form, $\alpha(h\nu) \sim (h\nu)^{-5/2}$, by the numerical one-parameter fitting. By adding this background absorption to the supercell MD results, we can obtain a combined x-ray absorption spectra of dense silicon plasmas in a much wider range of photon energies. To extend the K-edge tail to the several-keV range, we again take the single-atom absorption data fitted to the same analytic form. Accuracy of this simple analytic form was verified by comparison to the reference DFT data at selected thermodynamic conditions when it was possible to extend the Kubo–Greenwood calculations to the 10-keV photon energy range. The standard bremsstrahlung absorption high-photon energy asymptotes decay faster, $\alpha(h\nu) \sim (h\nu)^{-3}$, and should be applicable at a significantly higher photon energy range. Extrapolation to the photon energy range above 10 keV with such simple analytic forms may introduce significant errors and require further investigation.

Accuracy of the proposed methodology is confirmed by the comparison shown in Fig. 1(c) for warm dense silicon at $\rho = 8.0$ g/cm^3 and $T = 1$ MK in which the number of bands included in supercell MD calculations is enough to close the gap between L and K edges and continuously cover the photon energy range up to $h\nu \sim 3.5$ keV. The combined data lie right on the top of the supercell MD reference results. To further validate our method, we performed combined calculations for the x-ray absorption spectra of silicon at ambient conditions ($\rho = 2.33$ g/cm^3 and $T = 300$ K). The results are shown in Fig. 1(d) demonstrate very good agreement between our calculation results and NIST reference data [49] in the x-ray photon energy range. Note that the discrepancy for $h\nu < 30$ eV outside of our x-ray photon energy range of interest is due to a known shortcoming of semi-local type of exchange-correlation (XC) functional used in calculations that tends to underestimate the electronic band gap and to overestimate the low-energy dynamic electrical conductivity and absorption [50]. Standard isolated atomic models based on the non-local Hartree-Fock approximation are free of self-interaction errors, provide realistic

band gap predictions, therefore are capable to bring the simulations for absorption at low energies very close to the experimental data [48].

Preliminary calculations of low-density iron opacity at stellar interior temperatures indicate that the proposed methodology is applicable to higher-Z [than Si] materials and can provide reliable results.

III. COMPUTATIONAL DETAILS

Using this justified and computationally feasible method, we perform *first-principles* studies on the x-ray absorption properties of silicon in a wide range of densities from 0.5 to 500 g/cm^3 and temperatures of 5×10^3 to 10^7 K. It is noted that our AIMD simulations were driven by the Kohn–Sham DFT forces for temperatures up to 250 kK, while the orbital-free DFT forces [51] are used for high-T up to 10 MK. Kubo–Greenwood optical calculations were performed on a set of five statistically independent snapshots selected along obtained AIMD trajectories using ABINIT [52–54] and KGEC@QUANTUM-ESPRESSO [51, 55, 56] packages (two packages were used for a cross-check). Thermal XC effects that are important in the warm dense matter (WDM) regime [57–59] were taken into account via Karasiev-Dufty-Trickey (KDT16) generalized gradient approximation (GGA) level XC functional with explicit temperature dependence [60]. DFT usually underestimate the absolute location of the K edge due to self-interaction errors. For silicon at ambient conditions this underestimation is about 100 eV. Results presented below are not corrected for this constant shift. Calculations on isolated Si ions required as input for some IPD models were carried out using diatomic molecule code [61].

A. *Ab-initio* molecular dynamics simulations

We used two forms of *ab-initio* molecular dynamics (AIMD) simulations, one driven by orbital-based Kohn–Sham (KS) density functional theory (DFT) forces, and one with the use of orbital-free (OF) DFT forces. KS-AIMD simulations for density range between 0.5 g/cm^3 and 50 g/cm^3 and for temperatures between 5 kK and 250 kK were done using the Vienna *ab-initio* simulation package (VASP) [62–64] with the 12 active electrons PAW data set modeling the electron–ion electrostatic interaction and the Perdew–Burke–Ernzerhof (PBE) exchange-correlation (XC) functional [65]. The number of atoms in simulation cell was varied (depending on material density) between 8 and 64. The real-space cell size in all cases was large enough to employ a Γ-point sampling of the Brillouin zone. Convergence with respect to the plane-wave energy cutoff was reached at 2000 eV. The number of thermally occupied bands included in the calculation, depending on thermodynamic conditions, varied between 500 and 4100, such that the smallest occupation number did not exceed 10^{-5} reaching convergence. The MD time step varied between 0.085 fs and 1.5 fs; the total number of MD steps was at least 1200 [66].

At temperatures 500 kK and above we switched to the OF-AIMD simulations. The material density range in these simulations was extended up to 500 g/cm^3. The number of atoms in the simulation cell was between 8 and 512 with exceptions at low density and very high temperature when we verified that the finite-size effects for predicted optical properties are very small; simulations were performed using four atoms [see Sec. III C for finite-size convergence tests]. The singular electron–ion interaction was regularized via local pseudo potential (LPP) generated at each thermodynamic condition as described in Ref. [67]. This procedure uses the Thomas–Fermi noninteracting free-energy density functional [34]; therefore, for consistency the same approximation was used in our OF-AIMD simulations performed with the PROFESS@QUANTUM-ESPRESSO computational package [51]. High temperatures require the use of a small MD time step. In these simulations the time step was scaled as $\sim T^{-1/2}$ and the total number of MD steps was 16,000. It was found that the pressure differences between KS-AIMD and OF-AIMD at overlapping temperatures were within ∼1% (see details in Ref. [66]).

B. Kubo–Greenwood electrical and optical properties calculations

The electrical and optical properties at each thermodynamic condition are calculated for a set of fixed statistically independent ionic configurations (so-called snapshots) selected along molecular dynamics trajectory using the Kubo–Greenwood formulation implemented within the PAW formalism in ABINIT [52–54] and KGEC@QUANTUM-ESPRESSO [51, 55, 56] packages. An all-electron PAW data set was generated using the ATOMPAW code [68]. A small augmentation sphere radius, $r_{\rm PAW} = 0.20 a_0$ (where $a_0 = \hbar/(m_e e^2)$ is the Bohr radius; $a_0 = 1$ in the Hartree atomic units), and high cutoff energy of 27 keV were required to obtain convergence of optic properties in the x-ray photon energy range, which depend not only on low-energy occupied bands, but also on negligibly occupied or empty high-energy bands (see next Subsection for details). Thermal exchange-correlation effects were taken into account via the KDT16 GGA-level XC functional with explicit temperature dependence [60].

For this method to continuously cover photon energies up to the x-ray range, a large number of empty bands must be included into calculations in order to take into account all bound-bound, bound-free, and free-free tran-

sitions with non-negligible contributions. The maximum photon energy that could be covered by calculation with number of bands N is approximately given by the energy difference between the energy of the last band and energy of $1s$ states $h\nu_{\max} \approx \varepsilon_N - \varepsilon_{1s}$ (for the K-edge tail), and as a difference between the energy of the last band and energy of $2p$ states, $h\nu_{\max} \approx \varepsilon_N - \varepsilon_{2p}$, (for the L-edge tail). In the example shown in Figs. 1(a) and (b), the *single-atom-in-a-cell* calculation is performed with $N = 16384$ bands, $\varepsilon_N = 8451.10$ eV, $\varepsilon_{1s} = -1760.14$ eV, and $\varepsilon_{2p} = -72.52$ eV. Therefore, this calculation continuously covers the L-edge photon energies up to ∼8.5 keV and the K-edge tail is extended up to ∼10 keV, but we must keep in mind that the photon energy range above 8.5 keV does not include transitions from $2p/2s$ to the high-energy continuum states (the L-edge tail). The Fermi level in this calculation is located near zero, so the free-free contributions are included approximately up to 8.5 keV. For the MD snapshot calculation with 32 atoms to cover the same range of the photon energies, the required number of bands is approximately 32× larger, i.e., such a calculation will require more than 500,000 bands, an absolutely unfeasible calculation. The methodology presented in Sec. II, based on the combination of the usual super-cell MD snapshotted results with a *single-atom-in-a-cell* calculation, is aimed to overcome this difficulty.

Kubo–Greenwood calculations on a uncorrelated sample set of five fixed ionic configurations selected along molecular dynamics trajectory were performed with a number of bands between 3072 and 16384, depending on the material density and number of atoms in simulation cell, and Baldereschis mean value point (BMVP) [69]. The *single-atom-in-a-cell* calculations were performed with a number of bands between 4096 and 16384, BMVP sampling for low material density, and up to $5 \times 5 \times 5$ Monkhorst–Pack k grid [70] at an elevated density. The Gaussian broadening was done with $\delta = 4$ eV in the case of super cell calculations, and δ between 20 and 80 eV in the case of the *single-atom-in-a-cell* calculations.

The frequency-dependent real part of electric conductivity, $\sigma_1(\omega)$, the real part of the index of refraction, $n(\omega)$, the absorption coefficient, $\alpha(\omega) = \sigma_1(\omega)\frac{4\pi}{n(\omega)c}$ (where c is the speed of light), and the mass-absorption coefficient $\alpha_{\rm m}(\omega) = \alpha(\omega)/\rho$ were calculated and averaged over a selected set of uncorrelated snapshots. Eventually the grouped Rosseland and Planck mean opacities for a group of photon energies between $\hbar\omega_1$ and $\hbar\omega_2$ were calculated as follows

$$\kappa_{\rm R}(\omega_1 : \omega_2) = \frac{\int_{\omega_1}^{\omega^2} n^2(\omega)\frac{\partial B(\omega,T)}{\partial T}{\rm d}\omega}{\int_{\omega_1}^{\omega^2} n^2(\omega)\alpha_{\rm m}^{-1}(\omega)\frac{\partial B(\omega,T)}{\partial T}{\rm d}\omega}\,, \qquad (1)$$

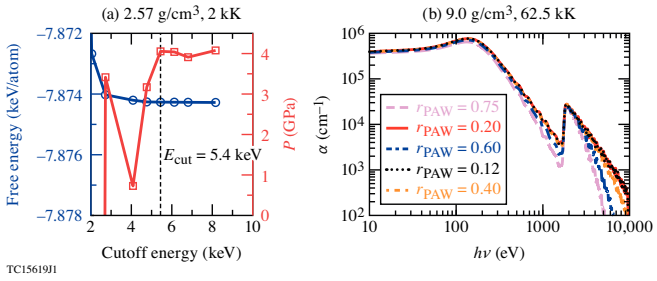

FIG. 2: (a) Convergence of the electronic free-energy and electronic pressure with respect to the energy cutoff for an *all-electron* PAW data set with cutoff radius $r_{\rm PAW} = 0.75a_0$ performed for a MD snapshot of Si using a 64-atom simulation supercell at $\rho_{\rm Si} = 2.57$ g/cm^3 and $T = 2000$ K. (b) Convergence of the L-edge and K-edge tail absorption coefficient with respect to the PAW cutoff radius for Si single-atom in simulation cell at $\rho_{\rm Si} = 9.0$ g/cm^3 and $T = 62500$ K.

and

$$\kappa_{\rm P}(\omega_1 : \omega_2) = \frac{\int_{\omega_1}^{\omega^2} n^2(\omega)\alpha_{\rm m}(\omega)B(\omega,T){\rm d}\omega}{\int_{\omega_1}^{\omega^2} n^2(\omega)B(\omega,T){\rm d}\omega}\,, \qquad (2)$$

where the Planck function $B(\omega,T) = (\hbar\omega^3/4\pi^3c^2)/(e^{\hbar\omega/k_{\rm B}T} - 1)$ depends on the photon frequency and the plasma temperature. The total mean opacity is obtained by integration between $\omega_1 = 0$ and $\omega_2 = \infty$.

C. All-electron projector augmented wave data sets

Calculation of optical properties including x-ray range involves transitions between the deep core states and partially occupied/unoccupied high-energy bound and free states. Therefore explicit consideration of $1s$ electrons in electronic structure calculations is required, which can only be done with use of an all-electron pseudopotential. The code ATOMPAW [68] was used to generate the all-electron (14 active electrons) PAW data sets with the PAW cutoff radius between $r_{\rm PAW} = 0.75a_0$ and $0.12a_0$. Explicit inclusion of core electrons in the self-consistent electronic structure calculation allows treatment of deeply bounded core electrons in an equal footing with valence and free electrons in the system. In this way the effects of environment on core electrons at extreme conditions of high density and temperature are taken into account on the self-consistent way during the electronic structure calculations and do not require any additional considerations on the used PAW data set due to particular thermodynamic conditions. The *all-electron* character and small cutoff radius are the only conditions required for transferability of a PAW data set generated at $T = 0$ K to extreme conditions of high temperature and high density. An example of such transferability was

discussed in Ref. [59], see Table I of this reference for comparison between the zero-T PAW data set and bare-Coulomb calculations at high temperatures.

Figure 2(a) shows the electronic free-energy and electronic pressure convergence with respect to the energy cutoff for the "soft" PAW data set with $r_{\rm PAW} = 0.75a_0$. The total electronic energy converges to less than 0.01 eV/atom at $E_{\rm cut} = 5.4$ keV, wherein the electronic pressure convergence error is ≈1%. Electronic energy and pressure depend on thermally occupied orbitals only. Calculation of properties that involve high-energy unoccupied orbitals may converge differently with respect to the energy cutoff and/or $r_{\rm PAW}$ value. An energy cutoff convergence study was performed for each set of PAW data with $r_{\rm PAW} = 0.75$, 0.60, 0.40, 0.20 and 0.12 of the Bohr radius a_0; in further calculations we used $E_{\rm cut} = 11$, 11, 22, 27 and 76 keV, respectively. The total electronic energy and pressure change within above mentioned convergence errors when calculated with each of these harder PAW data set. Figure 2(b) shows convergence of the absorption coefficient of silicon plasmas at $\rho = 9.0$ g/cm^3 and $T = 62500$ K with respect to the $r_{\rm PAW}$ value. It is evident that soft PAW data sets with $r_{\rm PAW} \leq 0.40a_0$ do not provide convergence of the absorption coefficient for the L-edge and K-edge tails. PAW data sets with a large cutoff radius predict smooth $1s$, $2s$, and $2p$ core pseudo-orbitals. The PAW formalism may not restore accurately the all-electron nature of these orbitals if an insufficient number of additional partial waves is included in the generation procedure. As a result, the matrix elements between too-smooth deep core bands and high-energy free states can be strongly underestimated. A small augmentation sphere radius, $r_{\rm PAW} = 0.20a_0$, and high cutoff energy of 27 keV are required to avoid such an underestimation of matrix elements between the deep bound and high-energy continuum states.

To estimate the magnitude of finite-size effects on the absorption coefficient when the number of atoms in a simulation cell is reduced at high temperatures, we performed a series of tests for silicon plasmas at selected densities and a few elevated temperatures. Figure 3 shows the absorption coefficient as a function of photon energy for two system sizes at two representative density and temperature conditions. Changing the number of atoms from $N = 32$ to $N = 16$ at $\rho_{\rm Si} = 9.0$ g/cm^3 and $T = 0.5$ MK shown in Figs. 3(a) and 3(b) does not demonstrate any visible difference. Variation in N from eight to four atoms in a simulation cell shown in Figs. 3(c) and 3(d) introduces small oscillations of the absorption coefficient near $1s \rightarrow 2p$ line and the K edge. Therefore, all our results are from converged calculations with $N \geq 8$ with few exceptions at low density and very high temperature when the system size was reduced to four atoms in simulation cell without introducing significant errors.

IV. RESULTS

A. Intrinsic atomic physics behind x-ray absorption line shifts

From our systematic calculations of the absorption coefficient for silicon plasmas, we present the interesting physics findings at representative WDM conditions. We first illustrate the detailed transition features revealed by our computational method in Fig. 4, which shows the mass absorption coefficient of silicon at $\rho = 0.5$ g/cm^3 and $T = 250$ kK and the corresponding density of states (DOS). Figures 4(b) and 4(d) display that deep core states are located at near $E = -1810$ eV, -160 eV, and -117 eV, corresponding to $1s$, $2s$, and $2p$ bands, respectively. Above the Fermi level there are three broad peaks that could be identified as the density of $3s$, $3p$, and $4s$+$3d$ states; these peaks integrate to give 2, 6, and about 12 total states correspondingly, which were shown as jumps in the integrated DOS illustrated in Fig. 4(d) by the solid red curve. The energy differences between these states allow us to identify the absorption peaks that appeared in Fig. 4(a) as follows (from low to high photon energy): (i) $2s \rightarrow 2p$ *intra-shell* absorption at near 45 eV; (ii) strong $2p \rightarrow 3s$ pre-edge absorption at 100 eV; (iii) the L-edge at near 120 eV; (iv) $2s \rightarrow 3p$ post-edge peak at near 150 eV; (v) strong $1s \rightarrow 2p$ line at near 1690 eV; (vi) weak dipole-forbidden $1s \rightarrow 3s$ absorption at near 1780 eV; (vii) a very strong $1s \rightarrow 3p$ pre-edge peak at 1800 eV; and eventually the K edge near 1815 eV.

The $2s \rightarrow 2p$ *intra-shell* and $1s \rightarrow 2p$ absorption arise due to the depletion of $2p$ states. The dipole-forbidden $1s \rightarrow 3s$ contribution appears because the final $3s$ states lose their strict spherical symmetry in dense plasma due to interaction with closest neighboring ions, similar to the distortion of $2s$ states occurring in superdense plasmas [71]. The elevated temperature makes ions approach each other over to significantly smaller distances as compared to distances defined by the ionic Wigner–Seitz radius, thereby increasing the distortion of bound states. At higher density and temperature (10 g/cm^3 and 4 MK), deeper $2s$ states can even become distorted and a relatively stronger $1s \rightarrow 2s$ absorption peak at ∼1730 eV is observed, see Fig. 6 below. It is important to notice that atomistic spectroscopic models in principle cannot predict such a kind of dipole-forbidden transition without artificial distortion of atomic orbitals. We also notice that the Fermi level shown in Fig. 4(d) is located in between L-shell and M-shell states, hence the frequently used formula for the K-edge location as an energy difference between the Fermi level and the $1s$ state, $E_{\rm K} = E_{\rm F} - \varepsilon_{1s}$ may underestimate the K-edge energy by about 50 eV for the conditions shown in Fig. 4.

To study how the warm-dense-plasma environment affects the ionization potential of bound electrons and the

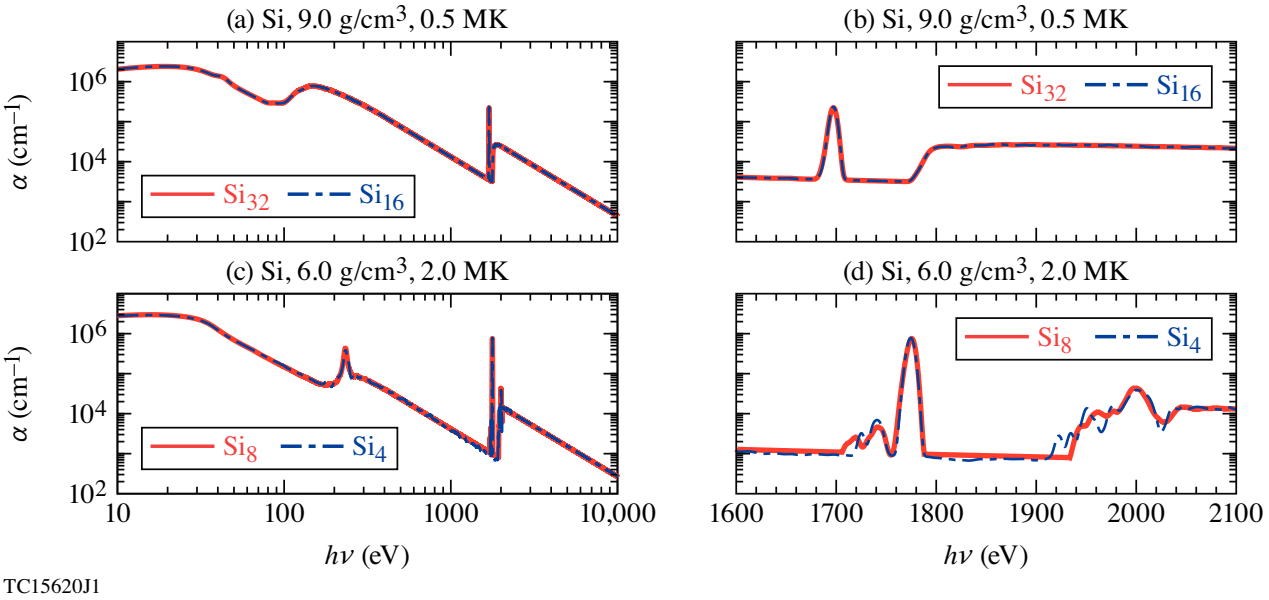

FIG. 3: Convergence of the absorption coefficient with respect to the system size for silicon plasmas: [(a),(b)] at $\rho = 9.0$ g/cm^3 and $T = 0.5$ MK and [(c),(d)] at $\rho = 6.0$ g/cm^3 and $T = 2.0$ MK.

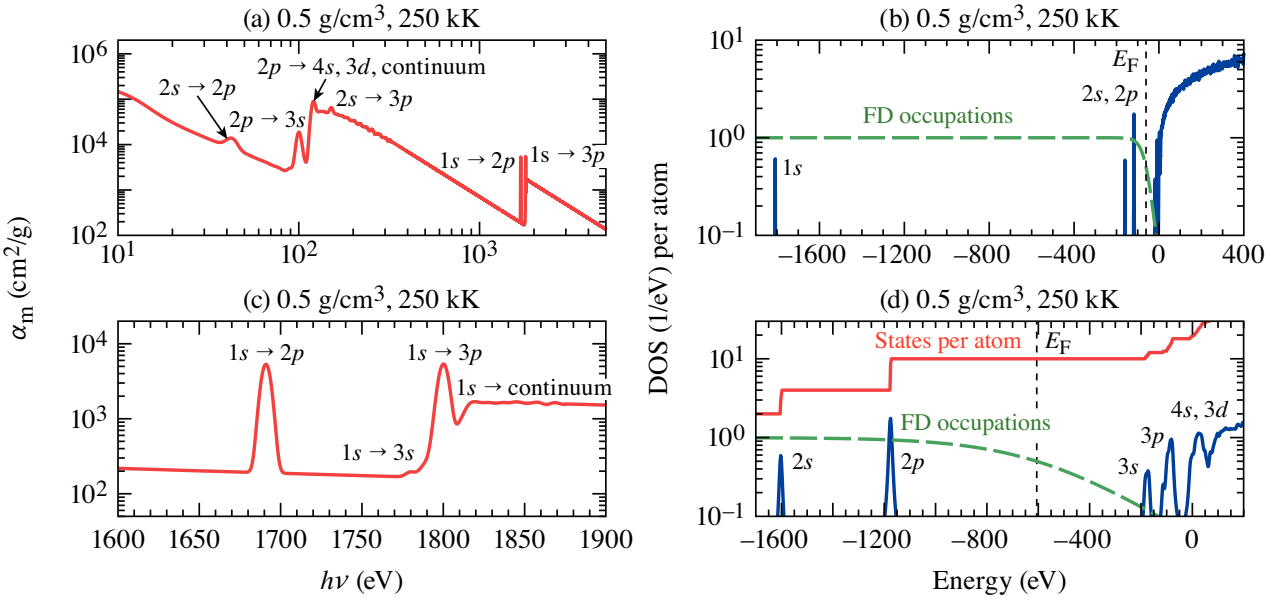

FIG. 4: [(a)] Mass absorption coefficient of silicon plasmas at $\rho = 0.5$ g/cm^3 and $T = 250$ kK. [(b)] Corresponding density of states (solid blue curve), Fermi–Dirac occupations (dashed green curve) and integrated density of states (solid red curve). [(c), (d)] Zoomed-in pictures of (a) and (b) near the K edge.

respective location of the K-edge and $1s \rightarrow 2p$ absorption, we consider two thermodynamic paths along an isotherm of $T = 500$-kK and along two isochores of $\rho = 10.0$-g/cm^3 and 35.0-g/cm^3 of silicon. Results for the absorption spectra and DOS for the 500-kK isotherm are shown in Fig. 5. The right panels of Fig. 5 indicate how the DOS evolves with increasing ρ. Quasi-static pressure broadening due to interaction with neighboring ions and respective shift of energy on individual ions is observed for both the K- and L-shell states (see also right panels of Figs. 6 and 7 below which show similar broadening). L-shell states can be much more easily disturbed; as a

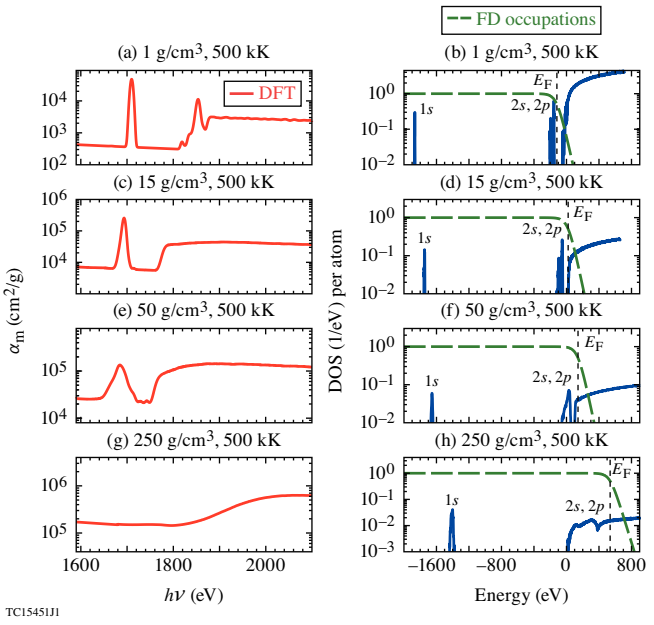

FIG. 5: Mass absorption coefficient and density of states of silicon plasmas along the $T = 500$ kK isotherm.

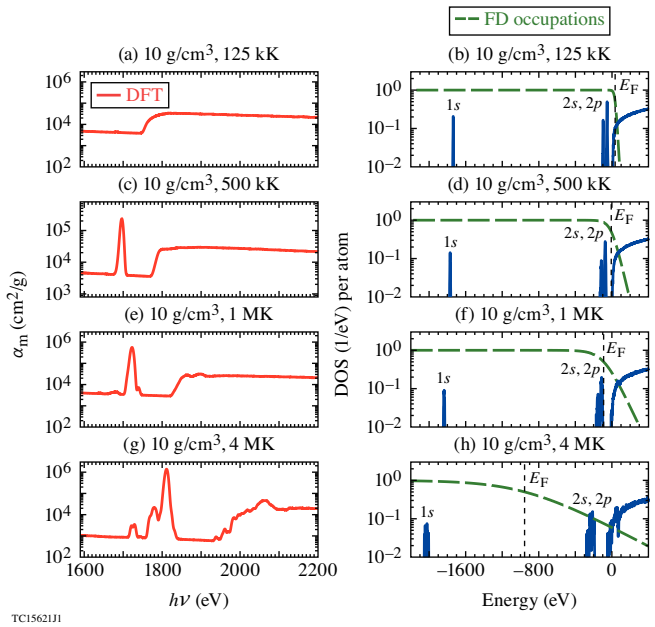

FIG. 6: Mass absorption coefficient and density of states of silicon plasmas along the $\rho = 10$-g/cm^3 isochore.

result, the $2s$ and $2p$ DOS peaks, being narrow and separated at 1 g/cm^3, eventually become broad and merge together at 50 g/cm^3. Figure 5(g) shows that the K-edge at 250 g/cm^3 becomes very smooth not only because of the $1s$ state broadening, but also due to the fact that the Fermi level moved completely into the continuum, such that the K-edge absorption gradually increases as the population of continuum states near the Fermi level and related Pauli blocking decrease.

As what one observes from the right panels of Fig. 5, the energies of the $1s$, $2s$, $2p$, and outer-shell near-free electrons move up overall due to the enhanced screening by free electrons and the increasing ion–ion interaction (caused by material density increase). However, the locations of the K edge and $1s \rightarrow 2p$ absorption lines first move toward low photon energies ("red shift"), then they have a "blue shift" toward larger photon energies for densities of $\rho > 50.0$ g/cm^3 [Fig. 5(g)]. In this case the broadening becomes important where the edge and peak structures start to disappear.

A similar situation occurs to the K-edge and K-L absorption along an isochoric thermodynamic path. Figures 6 and 7 show results for the absorption spectra and density of states for two isochores, $\rho = 10$ g/cm^3 and 35 g/cm^3. Along this thermodynamic path, the temperature-induced ionization decreases the screening by bound electrons, which cannot be compensated by increased free-electron screening, leading to downward movement of bound states, growth of the ionization potential and shift of the locations of the K-edge and $1s \rightarrow 2p$ absorption lines.

These shifts for the $T = 500$-kK isotherm are summa-

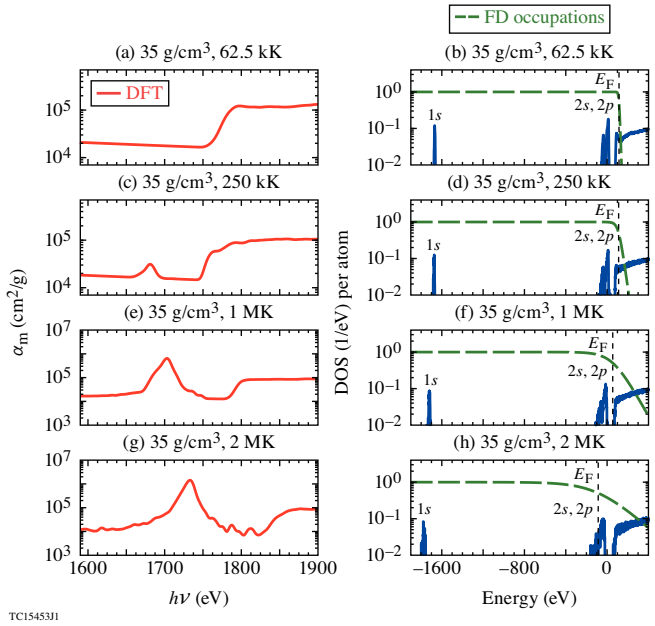

FIG. 7: Mass absorption coefficient and density of states of silicon plasmas along the $\rho = 35$-g/cm^3 isochore.

rized in Fig. 8(a) for different silicon densities [solid and dashed red curves (circles) labeled "DFT (this work)"], where the solid and dashed horizontal lines refer to the K edge and $1s \rightarrow 2p$ locations for silicon at ambient density 2.33 g/cm^3 and $T = 500$ kK. It is clearly seen that both absorption lines have the similar trend of red-to-blue shift as ρ increases. This behavior underlines the competition between electron screening and ion–ion in-

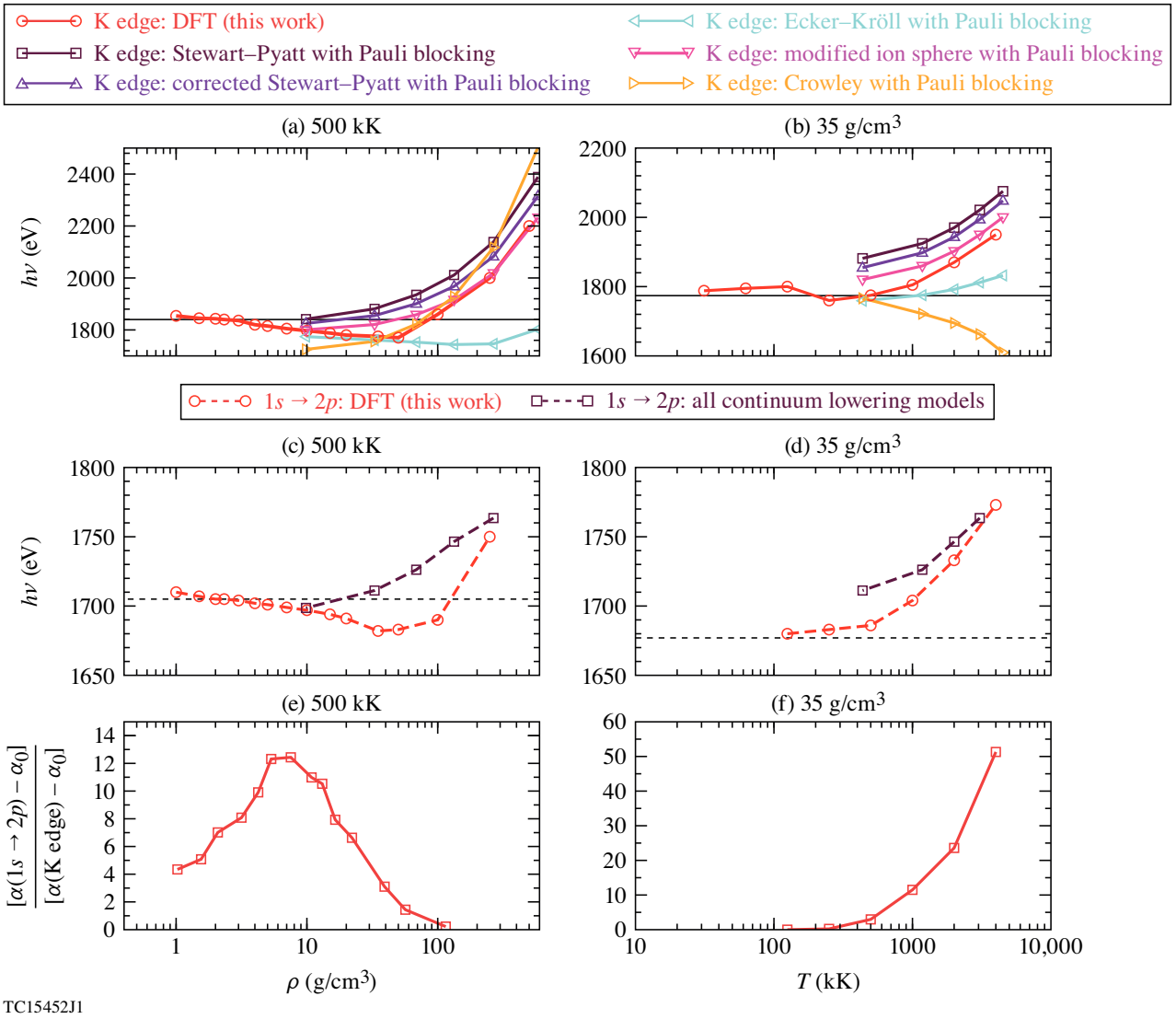

FIG. 8: [(a),(c)] Pressure-induced effect on the K edge and 1s → 2p absorption lines in silicon plasmas along the T=500-kK isotherm. [(b),(d)] Temperature-induced effect on the K edge and 1s → 2p absorption line location in silicon plasmas along ρ = 35.0-g/cm^3 isochore. [(e)] The ratio of absorption coefficients between α(K-L) and α(K-edge) with subtracted L-tail background absorption, α_0, along T = 500-kK isotherm. [(f)] Similar to (e) for the ρ = 35.0-g/cm^3 isochore.

teraction effects on the deeply bound electrons and on the outer-shell electrons. Screening of the 1s electrons prevails up to $\rho \approx 50$ g/cm^3, causing the K edge to a red shift of ~80 eV, as shown in Fig. 8(a). Namely, the increased free-electron density enhances the screening effect on the deeply bounded 1s states so that their energy levels move up with a faster pace than that of 2p and the continuum edge [see Figs. 5(a)-5(c)]. Consequently, the energy gap between 1s and 2p (between 1s and the continuum edge) decreases, leading to the observed "red shifts" of 1$s \rightarrow 2p$ transition and K edge. At higher densities of $\rho > 50$ g/cm^3, the L-shell electrons start to merge into the continuum [see Fig. 5(h)] due to density-induced ionization so that the "2s/2p" free-electron screening effect on the 1s state rises and the Fermi level moves up. Consequently, the 1$s \rightarrow 2p$ absorption line disappears and the K-edge shifts to larger $h\nu$ (blue shift) due to Pauli blocking, as shown in Fig. 8(a).

Recently, energy shifts of the iron K edge and fluorescence lines were measured experimentally [32]. A good agreement was found with shifts predicted by a DFT-based average-atom self-consistent field model (which includes free-electron screening) and disagreement with several IPD models. This DFT-based average atom model predicts redshifts in K_α and blue shifts in K_β due to decreasing screening from bound electrons. The iron K-edge shift is desrcibed by the model quite well. This shift reflects the interplay between the changes of 1s states binding energy due to the free-electron screening and changes in the Fermi energy.

Figure 8(b) shows results for the ρ = 35-g/cm^3 isochore [solid and dashed red curves (circles) labeled "DFT (this work)"]. Along this thermodynamic path, the deeply bounded $1s$ states move down as temperature increases (recall Fig. 7) as a consequence of the decreased screening by upper-bound electrons [due to thermal-induced ionization]. As a result, the K-edge shifts upward overall, except for an ∼40 eV red-shift at temperatures between 125 kK and 250 kK, shown in Fig. 8(b); meanwhile, the $1s \rightarrow 2p$ absorption line exhibits a monotonic blue shift.

To further understand these interesting features, we examine the widely used continuum-lowering models. These plasma-physics models predict the IPD for a given plasma condition (density, temperature, and an ion charge state $\bar{Z}$) with respect to an isolated ion. Calculations of charge states at each density/temperature condition were performed with the semi-classical finite-temperature Thomas–Fermi model [34], and the IPD was calculated as predicted by each of the models used. DFT calculations on isolated Si ions in charge states between +1 and +10 were carried out using a diatomic molecule code [61] to find the location of $1s$ and $2p$ states (the same KDT16 XC functional [60] was used for consistency with our extended system calculations). The K-edge location was calculated, taking into account the Pauli blocking, as a difference between the Fermi energy and the isolated ion $1s$ one-electron energy corrected by the IPD value as predicted by each model. A similar procedure can be applied to the $1s \rightarrow 2p$ line location. In this case the IPD, applied to both $1s$ and $2p$ states, cancels out, leading to the same result for all models: $E_{1s\rightarrow 2p} = \varepsilon^0_{2p} - \varepsilon^0_{1s}$, where ε^0_i are one-electron energies of the isolated ion in a given charge state. Energy of the $1s \rightarrow 2p$ absorption line calculated this way along the T = 500-kK isotherm and along the ρ = 35-g/cm^3 isochore is shown in Figs. 8(a) and 8(b) by the maroon dashed line (squares).

Figure 8(a) indicates that the atomic models of Stewart–Payatt [24], corrected Stewart–Pyatt [72], modified ion-sphere [73], and Crowley [74] fail to predict the K-edge red shift, providing only a qualitatively correct trend for the blue shift occurring at $\rho > 50$ g/cm^3. The finding that the Stewart–Pyatt model augmented with the Fermi surface rise provides a qualitatively correct blue-shift prediction has been presented earlier in Refs. [17, 18, 25]. Overall, the $1s \rightarrow 2p$ absorption line and K-edge locations predicted by these continuum-lowering models quantitatively disagree with DFT calculations. Specifically, the red shifts predicted by our DFT calculations are not seen by most of these continuum-lowering models. Ecker–Kröll [23] model predicts the red shift along the 500-kK isotherm, which is in a good agreement with our reference DFT calculations up to only $\rho \approx 50$ g/cm^3, then it deviates.

A nl quantum number dependent continuum-lowering model for hot plasmas, recently developed in Ref. [75], represents a fourth-order analytic approximation of the arbitrary perturbation potential method APPM [76]. This model demonstrated excellent agreement with the reference multi-configurational Dirac–Fock self-consistent finite-temperature ion sphere (MCDF-SCFTIS) calculations and the measured data in hot (above 600 eV) solid-density Cl plasmas. This analytic approach generalized for a N-bound-electron system and described in terms of scaled H-like nl quantum number dependent matrix elements is capable to correctly predict red shifts. However, this model was not tested in present work.

Finally, we plot the ratio of the $1s \rightarrow 2p$ absorption to the K-edge absorption coefficients in Figs. 8(c) and 8(d), as the function of thermodynamic conditions varies. Figure 8(c) shows this ratio peaks at $\rho \sim 5$ to 7 g/cm^3 for T = 500 kK, then decreases to zero as the density increases. For the constant density shown in Fig. 8(d), the ratio monotonically increases as plasma temperature goes high and high. Guided by such DFT calculations, one can measure this absorption ratio to infer the density and temperature conditions in experiments.

B. The FPOT of silicon for ICF and HEDP applications

In this section we present results of our systematic opacity calculations of silicon plasmas over a wide range of thermodynamic conditions for ICF and HEDP applications. The Si mass density was scanned from 0.5 g/cm^3 to 500 g/cm^3 with the temperature range between 5000 and 10,000,000 K. The *first-principles* DFT calculations are compared to the widely used astrophysics opacity tables (AOT) [77]. The AOT model is currently used in our hydrocodes to simulate ICF and HEDP experiments.

Figure 9 shows comparison between the grouped mean Rosseland opacities, $\kappa_{\rm R}$ defined by Eq. (1), from our *first-principles* DFT simulations and currently used AOT for silicon densities ρ = 0.5, 5 and 35 g/cm^3. At low density, ρ = 0.5 g/cm^3, both DFT and AOT opacities agree practically over entire range of photon energies at T = 250 kK. At all lower temperatures shown in Fig. 9, significant discrepancies are observed for low photon-energy groups of $h\nu < 200$ eV. When the mass density increases to 5 and 35 g/cm^3 the AOT opacity diverges from the reference DFT values in the same low photon-energy groups, for the photon-energy groups near K edge ($h\nu$ near 2 keV) at T = 4 MK, and for the photon-energy groups above ∼ 5 keV. Figure 10 shows similar comparisons for three higher material densities, 100, 250, and 500 g/cm^3. For ρ = 100 g/cm^3 at $T \geq 1$ MK the largest discrepancies occur again for the low photon-energy groups of $h\nu < 200$ eV. For ρ = 250 and 500 g/cm^3 the AOT model significantly underestimates opacity for the intermediate

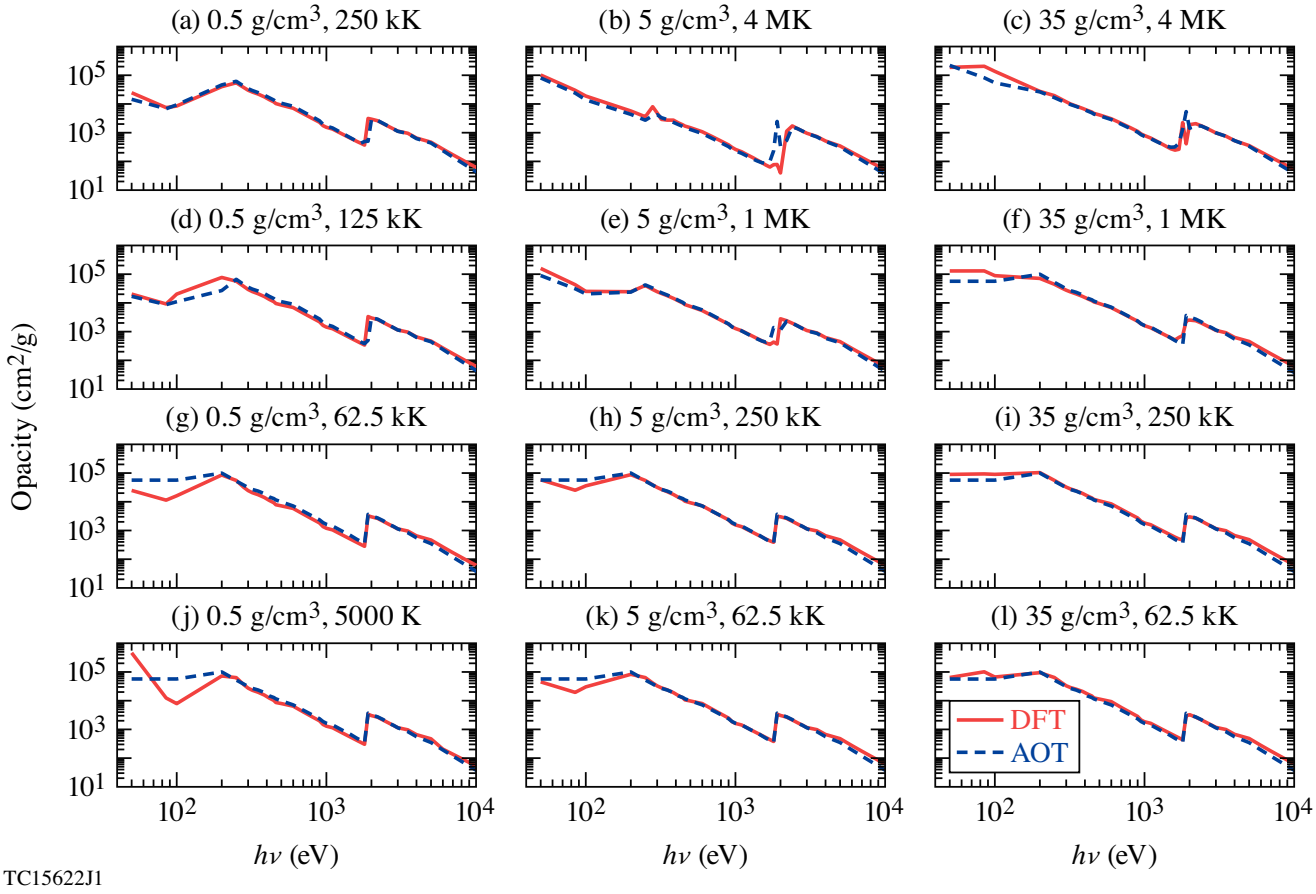

FIG. 9: Comparison of the 48-group mean Rosseland opacity between *first-principles* DFT and AOT as a function of the central photon energy in each group for silicon plasmas for $\rho = 0.5$, 5, and 35 g/cm^3 and selected temperatures.

range of photon-energy groups (between 200 and 2400 eV) and for high photon energies above 5 keV. Figure 10 shows other significant differences between DFT and AOT data: (i) AOT completely misses the K-edge shifting predicted by accurate DFT simulations; (ii) the silicon K edge, as predicted by DFT simulations, gradually becomes smooth as the plasma temperatures increases (see corresponding discussion in Sec. IV A), while the AOT model gives much sharper K-edge.

The total opacities from our DFT and AOT calculations are further compared in Fig. 11. The total/gray Rosseland mean opacity $\kappa_{\rm R}$ of Si is shown as a function of temperature for three representative cases $\rho = 5$, 35 and 250 g/cm^3. Both DFT and AOT total opacities agree well for temperatures above few tens of eV; however, the AOT model significantly underestimates the total opacity for $\rho = 5$ at temperatures below 10 eV. This finding is similar to the comparison between DFT and AOT for CH plasmas [15]. For densities $\rho = 35$ and 250 g/cm^3 at low temperatures (near 10 eV and below) the AOT total opacities are higher than the reference DFT values.

V. SUMMARY AND CONCLUSIONS

In conclusion, a novel free-energy DFT-based methodology has been developed that enables us to perform *first-principles* calculations of x-ray absorption in warm dense mid-/high-Z plasmas for a wide range of photon energies and plasma conditions. Applying the developed method to warm dense silicon plasmas, we revealed interesting red-to-blue shifts of K-edge and K-L absorptions, which are further explained by the competition between the free-electron screening to the K-shell core electrons and the screening of outer L-shell and M-shell electrons. The red-to-blue shift change occurs when the L- and M-shell electrons start to merge into continuum rising the free-electron screening to K-shell core and moving the Fermi level further up. It is noted that the DFT-predicted red shifts are missing in most traditional continuum-lowering models, except for the Ecker–Kröll model. Other continuum-lowering models provide only a qualitative agreement on the blue-shift magnitude.

Observing the fact that the relative magnitude of the K-L and K-edge absorption strongly depend on plasma environment, we propose using the ratio of $1s \rightarrow 2p$ ab-

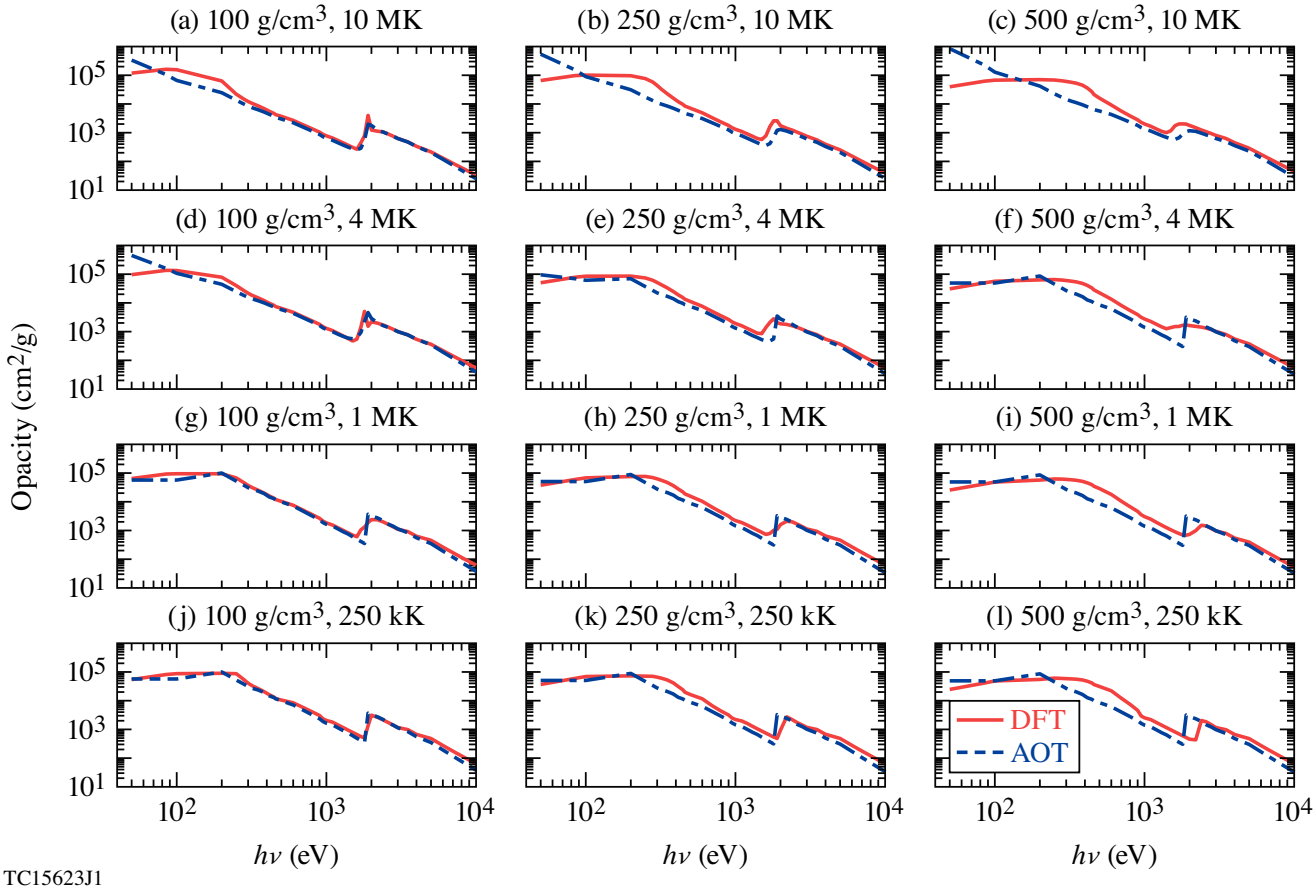

FIG. 10: Comparison of the 48-group mean Rosseland opacity between *first-principles* DFT and AOT as a function of the central photon energy in each group for silicon plasmas for $\rho = 100$, 250 and 250 g/cm^3 and selected temperatures.

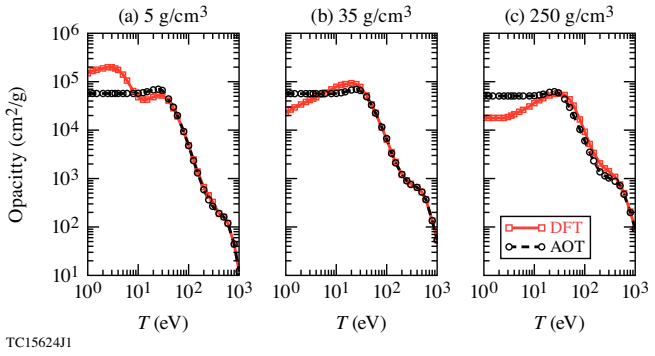

FIG. 11: Total Rosseland mean opacity of silicon at $\rho = 5$, 35 and 250 g/cm^3 as a function of temperature as predicted by our *first-principles* DFT calculations and AOT model.

sorption to the K-edge absorption to characterize the thermodynamic properties of dense plasmas through the x-ray spectroscopy technique.

Given the lack of HED experimental measurements of Si opacities, we hope our *ab initio* results provide reference data for future improvements to atomic-physics–based opacity models used in astrophysics and HED physics, as well as to continuum-lowering models in plasma physics. Novel methodology developed in this work was applied for systematic calculations of absorption and mean grouped opacity of silicon plasmas in a wide range of thermodynamic conditions. The resulting FPOT data were compared with the widely used AOT model. We found significant quantitative and qualitative discrepancies. We anticipate that these discrepancies will affect the radiation transport in simulations of ICF implosion targets with Si-doped ablators and related HEDP experiments.

VI. ACKNOWLEDGMENTS

This material is based upon work supported by the Department of Energy National Nuclear Security Administration under Award Number DE-NA0003856, U.S. National Science Foundation PHY Grant No. 1802964, the University of Rochester, and the New York State Energy Research and Development Authority.

This report was prepared as an account of work spon-

This research used resources of the National Energy Research Scientific Computing Center, a DOE Office of Science User Facility supported by the Office of Science of the U.S. Department of Energy under Contract No. DE-AC02-05CH11231.

[1] J.J. Fortney and N. Nettelmann, The Interior Structure, Composition, and Evolution of Giant Planets, Space Sci. Rev. **152**, 423-447 (2010).

[2] C.A. Iglesias, F.J. Rogers, and D. Saumon, Density Effects on the Opacity of Cool Helium White Dwarf, Astrophys. J. Lett. **569**, L111 (2002).

[3] S.X. Hu, L.A. Collins, V.N. Goncharov, T.R. Boehly, R. Epstein R.L. McCrory, and S. Skupsky, First-principles opacity table of warm dense deuterium for inertial-confinement-fusion applications, Phys. Rev. E **90**, 033111(1-10) (2014).

[4] S.X. Hu, V.N. Goncharov, T.R. Boehly, R.L. McCrory, S. Skupsky, L.A. Collins, J.D. Kress, and B. Militzer, Impact of first-principles properties of deuteriumtritium on inertial confinement fusion target designs, Phys. Plasmas **22**, 056304 (2015).

[5] J. Colgan, *et al.* Light element opacities from ATOMIC, High Energy Density Phys. **9**, 369-374 (2013).

[6] C.A. Iglesias and F.J. Rogers, Opacities for the solar radiative interior, Astrophys. J. **371**, 408-417 (1991).

[7] Q. Porcherot, J.-C. Pain, F. Gilleron, and T. Blenski, A consistent approach for mixed detailed and statistical calculation of opacities in hot plasmas, High Energy Density Phys. **7**, 234239 (2011).

[8] C. Blancard, Ph. Cosse, and G. Faussurier, Solar mixture opacity calculations using detailed configuration and level accounting treatments, Astrophys. J. **745**, 10 (2012).

[9] D. Benredjem, W. Jarrah, F. Gilleron, J.-C. Pain, S. Ferri, A. Calist, Opacity calculations. Ge and Si dopants in ICF, High Energy Density Phys. **16**, 23 (2015);

[10] V. Dervieux, B.Loupias, S.Baton, L.Lecherbourg, K. Glize, C. Rousseaux, C. Reverdin, L. Gremillet, C. Blancard, V. Silvert, J.-C. Pain, C.R.D. Brown, P. Allan, M.P. Hill, D.J. Hoarty, P. Renaudin, Characterization of near-LTE, high-temperature and high-density aluminum plasmas produced by ultra-high intensity lasers, High Energy Density Phys. **16**, 12 (2015).

[11] S.J. Rose, Calculations of the radiative opacity of laser-produced plasmas, J. Phys. B: At. Mol. Opt. Phys. **25**, 1667-1681 (1992).

[12] S.J. Rose, New experimental possibilities for measuring radiative opacity under conditions in the sun's interior, Plasma Phys. Control. Fusion **47**, B735 (2005).

[13] D.J. Hoarty, J. Morton, M. Jeffery, L.K. Pattison, A. Wardlow, S.P.D. Mangles, S.J. Rose, C. Iglesias, K. Opachich, R.F. Heeter, T.S. Perry, A proposal to measure iron opacity at conditions close to the solar convective zone-radiative zone boundary, High Energy Density Phys. **32**, 70 (2019).

[14] J.E. Bailey, T. Nagayama, G.P. Loisel, G.A. Rochau, C. Blancard, J. Colgan, Ph. Cosse, G. Faussurier, C. J. Fontes, F. Gilleron, I. Golovkin, S.B. Hansen, C.A. Iglesias, D.P. Kilcrease, J.J. MacFarlane, R.C. Mancini, S.N. Nahar, C. Orban, J.-C. Pain, A.K. Pradhan, M. Sherrill, and B.G. Wilson, A higher-than-predicted measurement of iron opacity at solar interior temperatures, Nature (London) **517**, 56 (2015).

[15] S.X. Hu, L.A. Collins, J.P. Colgan, V.N. Goncharov, and D.P. Kilcrease, Optical properties of highly compressed polystyrene: An *ab initio* study, Phys. Rev. B **96**, 144203 (2017).

[16] S.X. Hu, Continuum Lowering and Fermi-Surface Rising in Strongly Coupled and Degenerate Plasmas, Phys. Rev. Lett. **119**, 065001 (2017).

[17] C.A. Iglesias and P.A. Sterne, Comment on "Continuum Lowering and Fermi-Surface Rising in Strongly Coupled and Degenerate Plasmas", Phys. Rev. Lett. **120**, 119501 (2018).

[18] S.X. Hu, Reply to "Comment on 'Continuum Lowering and Fermi-Surface Rising in Strongly Coupled and Degenerate Plasmas'", Phys. Rev. Lett. **120**, 119502 (2018).

[19] T. Nagayama, J.E. Bailey, G.P. Loisel, G.S. Dunham, G.A. Rochau, C. Blancard, J. Colgan, Ph. Cossé, G. Faussurier, C.J. Fontes, F. Gilleron, S.B. Hansen, C.A. Iglesias, I.E. Golovkin, D.P. Kilcrease, J.J. MacFarlane, R.C. Mancini, R.M. More, C. Orban, J.-C. Pain, M.E. Sherrill, and B.G. Wilson Systematic Study of *L*-Shell Opacity at Stellar Interior Temperatures, Phys. Rev. Lett. **122**, 235001(1-7) (2019).

[20] O. Ciricosta, S.M. Vinko, H.-K. Chung, B.-I. Cho, C.R.D. Brown, T. Burian, J. Chalupský, K. Engelhorn, R.W. Falcone, C. Graves, V. Hajková, A. Higginbotham, L. Juha, J. Krzywinski, H. J. Lee, M. Messerschmidt, C. D. Murphy, Y. Ping, D. S. Rackstraw, A. Scherz, W. Schlotter, S. Toleikis, J. J. Turner, L. Vysin, T. Wang, B. Wu, U. Zastrau, D. Zhu, R.W. Lee, P. Heimann, B. Nagler, and J. S. Wark, Direct Measurements of the Ionization Potential Depression in a Dense Plasma, Phys. Rev. Lett. **109**, 065002 (2012).

[21] S.M. Vinko, O. Ciricosta, B.I. Cho, K. Engelhorn, H.-K. Chung, C.R.D. Brown, T. Burian, J. Chalupský, R.W.

Falcone, C. Graves, V.Hájková, A. Higginbotham, L. Juha, J. Krzywinski, H.J. Lee, M. Messerschmidt, C.D. Murphy, Y. Ping, A. Scherz, W. Schlotter, S. Toleikis, J.J. Turner, L. Vysin, T.Wang, B.Wu, U. Zastrau, D. Zhu, R.W. Lee, P.A. Heimann, B. Nagler, and J. S.Wark, Creation and diagnosis of a solid-density plasma with an X-ray free-electron laser, Nature (London) **482**, 59-63 (2012).

[22] D.J. Hoarty, P. Allan, S.F. James, C.R.D. Brown, L.M.R. Hobbs, M.P. Hill, J.W.O. Harris, J. Morton, M.G. Brookes, R. Shepherd, J. Dunn, H. Chen, E. Von Marley, P. Beiersdorfer, H.K. Chung, R.W. Lee, G. Brown, and J. Emig, Observations of the effect of ionization-potential depression in hot dense plasma, Phys. Rev. Lett. **110**, 265003 (2013).

[23] G. Ecker and W. Kröll, Lowering of the ionization energy for a plasma in thermodynamic equilibrium, Phys. Fluids **6**, 62 (1963).

[24] J. C. Stewart and K. D. Pyatt, Jr., Lowering of ionization potentials in plasmas, Astrophys. J. **144**, 1203 (1966).

[25] F.B. Rosmej, Ionization potential depression in an atomic-solid-plasma picture, J. Phys. B: At. Mol. Opt. Phys. **51**, 09LT01(1-10) (2018).

[26] S.-K. Son, R. Thiele, Z. Jurek, B. Ziaja, and R. Santra, Quantum-Mechanical Calculation of Ionization-Potential Lowering in Dense Plasmas, Phys. Rev. X **4**, 031004(1-14) (2014).

[27] S.M. Vinko, O. Ciricosta, and J.S. Wark, Density functional theory calculations of continuum lowering in strongly coupled plasmas, Nat. Commun. 5:3533 doi:10.1038/ncomms4533 (2014).

[28] O. Ciricosta, S.M. Vinko, B. Barbrel, D.S. Rackstraw, T.R. Preston, T. Burian, J. Chalupský, B.I. Cho, H.-K. Chung, G.L. Dakovski, K. Engelhorn, V. Hájková, P. Heimann, M. Holmes, L. Juha, J. Krzywinski, R.W. Lee, S. Toleikis, J.J. Turner, U. Zastrau, and J.S. Wark, Measurements of continuum lowering in solid-density plasmas created from elements and compounds, Nat. Commun. 7:11713 doi: 10.1038/ncomms11713 (2016).

[29] S. Mazevet and G. Zeŕah, *Ab Initio* Simulations of the K-Edge Shift along the Aluminum Hugoniot", Phys. Rev. Lett. **101**, 155001 (2008).

[30] A. Benuzzi-Mounaix, F. Dorchies, V. Recoules, F. Festa, O. Peyrusse, A. Levy, A. Ravasio, T. Hall, M. Koenig, N. Amadou, E. Brambrink, and S. Mazevet, Electronic Structure Investigation of Highly Compressed Aluminum with K Edge Absorption Spectroscopy, Phys. Rev. Lett. **107**, 165006 (2011).

[31] S. Zhang, S. Zhao, W. Kang, P. Zhang, and X.-T. He, Link between K absorption edges and thermodynamic properties of warm dense plasmas established by an improved first-principles method, Phys. Rev. B **93**, 115114 (2016).

[32] S.B. Hansen, E.C. Harding, P.F. Knapp, M.R. Gomez, T. Nagayama, and J.E. Bailey, Changes in the electronic structure of highly compressed iron revealed by X-ray fluorescence lines and absorption edges, High Energy Density Phys. **24**, 39-43 (2017).

[33] N.D. Mermin, Phys. Rev. **137**, A1441 (1965).

[34] R.P. Feynman, N. Metropolis, and E. Teller, Equation of State of Elements Based on the Generalized Thomas-Fermi Theory, Phys. Rev. **75**, 1561 (1949).

[35] F. Perrot, Phys. Rev. A **20**, 586 (1979).

[36] V.V. Karasiev, T. Sjostrom, and S.B. Trickey, Phys. Rev. B **86**, 115101 (2012).

[37] V.V. Karasiev, D. Chakraborty, O.A. Shukruto, and S.B. Trickey, Phys. Rev. B **88**, 161108(R) (2013).

[38] K. Luo, V.V. Karasiev, and S.B. Trickey, A simple generalized gradient approximation for the noninteracting kinetic energy density functional, Phys. Rev. B **98**, 041111(R) (2018).

[39] M. Bethkenhagen, B.B.L. Witte, M. Schörner, G. Röpke, T. Döppner, D. Kraus, S.H. Glenzer, P.A. Sterne, and R. Redmer, Carbon ionization at gigabar pressures: An ab initio perspective on astrophysical high-density plasmas, Phys. Rev. Res. **2**, 023260 (2020).

[40] P. Audebert, P. Renaudin, S. Bastiani-Ceccotti, J.-P. Geindre, C. Chenais-Popovics, S. Tzortzakis, V. Nagels-Silvert, R. Shepherd, I. Matsushima, S. Gary, F. Girard, O. Peyrusse, and J.-C. Gauthier, Picosecond Time-Resolved X-Ray Absorption Spectroscopy of Ultrafast Aluminum Plasmas, Phys. Rev. Lett. **94**, 025004(1-4) (2005).

[41] A. Mancić, A. Lévy, M. Harmand, M. Nakatsutsumi, P. Antici, P. Audebert, P. Combis, S. Fourmaux, S. Mazevet, O. Peyrusse, V. Recoules, P. Renaudin, J. Robiche, F. Dorchies, and J. Fuchs, Picosecond Short-Range Disordering in Isochorically Heated Aluminum at Solid Density, Phys. Rev. Lett. **104**, 035002(1-4) (2010).

[42] B. Mahieu, N. Jourdain, K. Ta Phuoc, F. Dorchies, J.-P. Goddet, A. Lifschitz, P. Renaudin, and L. Lecherbourg, Probing warm dense matter using femtosecond X-ray absorption spectroscopy with a laser-produced betatron source, Nat. Commun. 9:3276 doi: 10.1038//s41467-018-05791-4 (2018).

[43] B.I. Cho, K. Engelhorn, A.A. Correa, T. Ogitsu, C.P. Weber, H.J. Lee, J. Feng, P.A. Ni, Y. Ping, A.J. Nelson, D. Prendergast, R.W. Lee, R.W. Falcone, and P.A. Heimann, Electronic Structure ofWarm Dense Copper Studied by Ultrafast X-Ray Absorption Spectroscopy, Phys. Rev. Lett. **106**, 167601(1-4) (2011).

[44] Y. Ping, F. Coppari, D.G. Hicks, B. Yaakobi, D.E. Fratanduono, S. Hamel, J.H. Eggert, J.R. Rygg, R.F. Smith, D.C. Swift, D.G. Braun, T.R. Boehly, and G.W. Collins, Solid Iron Compressed Up to 560 GPa, Phys. Rev. Lett. **111**, 065501(1-5) (2013).

[45] R. Kubo, Statistical-Mechanical Theory of Irreversible Processes. I. General Theory and Simple Applications to Magnetic and Conduction Problems, J. Phys. Soc. Jpn. **12**, 570 (1957).

[46] D.A. Greenwood, The Boltzmann Equation in the Theory of Electrical Conduction in Metals, Proc. Phys. Soc. **71**, 585 (1958).

[47] R.J. Gould, K-shell photoionization of multielectron atomic system, AJ **235**, 650-664 (1980).

[48] M.Ya. Amus'ya, N.A. Cherepkov, L.V. Chernysheva, and S.I. Sheftel', Calculation of the photo-ionization cross section for argon in Hartree-Fock approximation, Sov. Phys. JETP **29**, 1018-1021 (1969).

[49] C.T. Chantler, K. Olsen, R.A. Dragoset, J. Chang, A.R. Kishore, S.A. Kotochigova, and D.S. Zucker, NIST Standard Reference Database 66, NIST.

[50] B.L. Witte, L.B. Fletcher, E. Galtier, E. Gamboa, H.J. Lee, U. Zastrau, R. Redmer, S.H. Glenzer, and P. Sperling, Warm Dense Matter Demonstrating Non-Drude Conductivity from Observations of Nonlinear Plasmon Damping, Phys. Rev. Lett. **118**, 225001(1-6) (2017).

[51] V.V. Karasiev, T. Sjostrom, and S.B. Trickey, Finite-temperature orbital-free DFT molecular dynamics: Coupling PROFESS and QUANTUM ESPRESSO, Comput. Phys. Commun. **185**, 3240 (2014).

[52] X. Gonze, B. Amadon, P.-M. Anglade, J.-M. Beuken, F. Bottin, P. Boulanger, F. Bruneval, D. Caliste, R. Caracas, M. Cote, T. Deutsch, L. Genovese, Ph. Ghosez, M. Giantomassi, S. Goedecker, D.R. Hamann, P. Hermet, F. Jollet, G. Jomard, S. Leroux, M. Mancini, S. Mazevet, M.J.T. Oliveira, G. Onida, Y. Pouillon, T. Rangel, G.-M. Rignanese, D. Sangalli, R. Shaltaf, M. Torrent, M.J. Verstraete, G. Zerah, and J.W. Zwanziger, Comput. Phys. Commun. **180**, 2582 (2009); X. Gonze, G.-M. Rignanese, M. Verstraete, J.-M. Beuken, Y. Pouillon, R. Caracas, F. Jollet, M. Torrent, G. Zerah, M. Mikami, Ph. Ghosez, M. Veithen, J.-Y. Raty, V. Olevano, F. Bruneval, L. Reining, R. Godby, G. Onida, D.R. Hamann, and D.C. Allan, A brief introduction to the ABINIT software package, Zeit. Kristallogr. **220**, 558 (2005).

[53] M. Torrent, F. Jollet, F. Bottin, G. Zerah, and X. Gonze, Implementation of the projector augmented-wave method in the ABINIT code: Application to the study of iron under pressure, Comput. Mat. Sci. **42**, 337 (2008).

[54] S. Mazevet, M. Torrent, V. Recoules, and F. Jollet, Calculations of the transport properties within the PAW formalism, High Energy Density Phys. **6**, 84 (2010).

[55] Paolo Giannozzi, Stefano Baroni, Nicola Bonini, Matteo Calandra, Roberto Car, Carlo Cavazzoni, Davide Ceresoli, Guido L. Chiarotti, Matteo Cococcioni, Ismaila Dabo, Andrea Dal Corso, Stefano de Gironcoli, Stefano Fabris, Guido Fratesi, Ralph Gebauer, Uwe Gerstmann, Christos Gougoussis, Anton Kokalj, Michele Lazzeri, Layla Martin-Samos, Nicola Marzari, Francesco Mauri, Riccardo Mazzarello, Stefano Paolini, Alfredo Pasquarello, Lorenzo Paulatto, Carlo Sbraccia, Sandro Scandolo, Gabriele Sclauzero, Ari P. Seitsonen, Alexander Smogunov, Paolo Umari, and Renata M. Wentzcovitch, QUANTUM ESPRESSO: a modular and open-source software project for quantum simulations of materials, J. Phys.: Condens. Matter **21**, 395502 (2009).

[56] L. Caldern, V.V. Karasiev, S.B. Trickey, KuboGreenwood electrical conductivity formulation and implementation for projector augmented wave datasets, Comput. Phys. Commun. **221**, 118-142 (2017).

[57] V.V. Karasiev, T. Sjostrom, J. Dufty, and S.B. Trickey, Accurate Homogeneous Electron Gas Exchange-Correlation Free Energy for Local Spin-Density Calculations, Phys. Rev. Lett. **112**, 076403 (2014).

[58] V.V. Karasiev, L. Calderín, and S.B. Trickey, Importance of finite-temperature exchange correlation for warm dense matter calculations, Phys. Rev. E **93**, 063207 (2016).

[59] V.V. Karasiev, S.X. Hu, M. Zaghoo, and T.R. Boehly, Exchange-correlation thermal effects in shocked deuterium: Softening the principal Hugoniot and thermophysical properties, Phys. Rev. B **99**, 214110(1-9) (2019).

[60] V.V. Karasiev, J.W. Dufty, and S.B. Trickey, Nonempirical Semilocal Free-Energy Density Functional for Matter under Extreme Conditions, Phys. Rev. Lett. **120**, 076401(1-7) (2018).

[61] A.N. Artemyev, E.V. Ludeña, V.V. Karasiev, and A.J. Hernández, A Finite B-Spline Basis Set for Accurate Diatomic Molecule Calculations, J. Comput. Chem. **25**, 368-374 (2004).

[62] G. Kresse and J. Hafner, Phys. Rev. B **47**, 558 (1993).

[63] G. Kresse and J. Hafner, Phys. Rev. B **49**, 14251 (1994).

[64] G. Kresse and J. Furthmüller, Phys. Rev. B **54**, 11169 (1996).

[65] J. P. Perdew, K. Burke, and M. Ernzerhof, Phys. Rev. Lett. **77**, 3865 (1996); *ibid* **78**, 1396(E) (1997).

[66] S.X. Hu, R. Gao, Y. Ding, L.A. Collins, and J.D. Kress, First-principles equation-of-state table of silicon and its effects on high-energy-density plasma simulations, Phys. Rev. E **95**, 043210 (2017).

[67] F. Lambert, J. Clérouin, and Gilles Zérah, Phys. Rev. E **73**, 016403 (2006).

[68] N.A.W. Holzwarth, A.R. Tackett, G.E. Matthewsa, A Projector Augmented Wave (PAW) code for electronic structure calculations, Part I: ATOMPAW for generating atom-centered functions, Comput. Phys. Commun. **135**, 329 (2001).

[69] A. Baldcreschi, Mean-value point in the Brillouin zone, Phys. Rev. B **7**, 5212 (1973).

[70] H.J. Monkhorst and J.D. Pack, Pack, Special points for Brillouin-zone integrations, Phys. Rev. B **13**, 5188 (1976).

[71] S.X. Hu, V.V. Karasiev, V. Recoules, P.M. Nilson, N. Brouwer, and M. Torrent, Interspecies radiative transition in warm and superdense plasma mixtures, Nat. Commun. 11:1989 doi: 10.1038/s41467-020-15916-3 (2020).

[72] B.J.B. Crowley, Continuum lowering - A new perspective, High Energy Density Phys. **13**, 84 (2014).

[73] D. Liberman and J. Albritton, Dense plasma equation of state model, J. Quant. Spectrosc. Radiat. Transfer **51**, 197 (1994).

[74] B.J.B. Crowley, Average-atom quantum-statistical cell model for hot plasma in local thermodynamic equilibrium over a wide range of densities, Phys. Rev. A **41**, 2179 (1990).

[75] X. Li, and F.B. Rosmej, Phys. Lett. A **384**, 126478 (2020).

[76] F. Rosmej, K. Bennadji, and V.S. Lisitsa, Phys. Rev. A **84**, 032512 (2011).

[77] W.F. Huebner, A.L. Merts, N.H. Magee, Jr., and M.F. Argo, Los Alamos National Laboratory, Los Alamos, NM, Report No LA-6760-M, 1977.